ACS NANO

www.acsnano.org

ARTICLE

Spin-Phonon Coupling in Iron-Doped Ultrathin Bismuth Halide Perovskite Derivatives

Yifeng Liu,[▽] Qing Ai,[▽] Gaihua Ye, Zhipeng Ye, Jakub Hrubý, Fan Wang, Tomas Orlando, Yuguo Wang, Jiaming Luo, Qiyi Fang, Boyu Zhang, Tianshu Zhai, Chen-yang Lin, Clyde Xu, Yifan Zhu, Tanguy Terlier, Stephen Hill, Hanyu Zhu,* Rui He,* and Jun Lou*

Cite This: *ACS Nano* 2024, 18, 12560−12568

Read Online

ACCESS | Metrics & More | Article Recommendations | Supporting Information

ABSTRACT: **Spin in semiconductors facilitates magnetically controlled optoelectronic and spintronic devices. In metal halide perovskites (MHPs), doping magnetic ions is proven to be a simple and efficient approach to introducing a spin magnetic momentum. In this work, we present a facile metal ion doping protocol through the vapor-phase metal halide insertion reaction to the chemical vapor deposition (CVD)-grown ultrathin Cs_3BiBr_6 perovskites. The Fe-doped bismuth halide (Fe:CBBr) perovskites demonstrate that the iron spins are successfully incorporated into the lattice, as revealed by the spin-phonon coupling below the critical temperature T_c around 50 K observed through temperature-dependent Raman spectroscopy. Furthermore, the phonons exhibit significant softening under an applied magnetic field, possibly originating from magnetostriction and spin exchange interaction. The spin-phonon coupling in Fe:CBBr potentially provides an efficient way to tune the spin and lattice parameters for halide perovskite-based spintronics.**

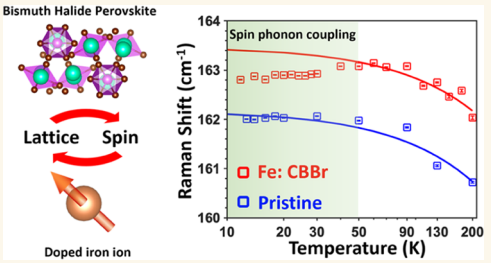

KEYWORDS: *cation doping, lead-free perovskites, magneto-Raman, spin-phonon coupling, temperature-dependent Raman, ultrathin crystals*

INTRODUCTION

Metal halide perovskites (MHPs) have become promising semiconductors in photonic and electronic research due to their superior optoelectronic properties including high carrier mobility and lifetime,[1] considerable carrier diffusion length,[2] and tunable band gap energies.[3] The recently observed spin−orbit coupling in MHPs showcased the spin-related properties including Rashba effects,[4] polarized light-dependent properties,[5] and magneto-optical effects.[6] In addition to the spin-dependent optical physics, spin-phonon coupling has garnered considerable attention owing to its implications in the fields of spintronics and multiferroics.[7−9] While the investigation of spin-phonon coupling has extensively focused on magnetic compounds such as $MnBi_2Te_4$[10] and Fe_3GeTe_2,[11] it has not received adequate attention in MHPs.

Spin-related properties support the evolution of the MHP-based optoelectronic,[12] spintronic,[13] and quantum anomalous Hall effect devices.[14] To meet the demand for rapid device development and following Moore's law, confining the MHP thickness to the nanoscale as well as its scalable synthesis become the priorities in the preparation of MHP-based materials. Chemical vapor deposition (CVD) methods provide a robust, controllable synthesis of ultrathin MHP-based materials and could enable large-scale device fabrication.[15,16] Our recent effort on the CVD growth of the ultrathin bismuth halide perovskites provides not only the desired platform for low-dimensional physics studies but also a possible solution to the substitution of the toxic lead with the more eco-friendly bismuth.[16] In addition to enable spin−orbit coupling, doping magnetic elements in the nonmagnetic MHPs turns out to be an efficient and straightforward strategy to demonstrate magnetic and other spin-related properties.[17,18] Through the magnetic element doping to the bismuth halide perovskite, we envision that the nonintrinsic spin-related properties such as the spin-phonon coupling could be induced in MHPs.

Multiple metal ion doping strategies have been well developed in MHPs and can be classified into two general

Received: March 7, 2024
Revised: April 10, 2024
Accepted: April 25, 2024
Published: May 3, 2024

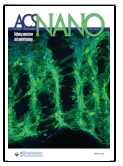

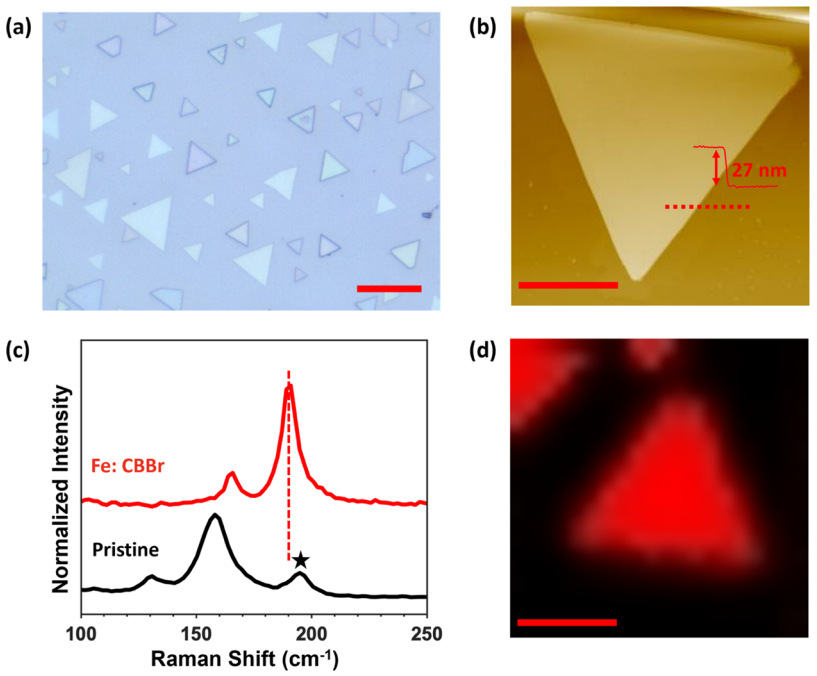

Figure 1. (a) Optical image of the CVD-grown Cs_3BiBr_6 flakes; scale bar: 50 μm. (b) AFM image of the CVD-grown Cs_3BiBr_6 flake; the inserted figure is the height profile; scale bar: 5 μm. (c) Room-temperature Raman spectra of the Fe:CBBr (3 h) (red) and pristine Cs_3BiBr_6 (black) perovskites. The star-marked peak at 194 cm^{-1} in the pristine spectrum comes from the fluorphlogopite mica (F:mica) substrate (Figure S2). The dashed red line highlights the peak in the Fe:CBBr perovskite, which is different from the peak of the substrate. (d) Raman mapping at 190 cm^{-1} of the Fe:CBBr perovskite; scale bar: 5 μm.

protocols, the one-step synthesis by directly introducing the metal ions in the precursors[19,20] and the postsynthetic treatment to dope the metal ions into the prepared parent perovskites.[21,22] The former protocol is mature for the bulk phase and nanocrystalline MHPs but becomes a challenge for the CVD-grown samples, where the growth process and product composition are not simply controlled by the stoichiometry ratio of the precursors. In comparison, the latter protocol, usually relying on the cation exchange process, can provide precise compositional control and preserve the geometry of the parent materials,[23] which are more desirable for the CVD-grown samples. Given the limited efforts in synthesizing ultrathin mixed *B*-site cation MHPs, there is clearly a need for efficient metal ion doping. This demand has sparked anticipation for the development of promising and facile postsynthetic methods.

Here, we report a facile metal ion doping strategy for CVD-grown ultrathin Cs_3BiBr_6 perovskite derivatives through postsynthetic metal halide vapor treatment. Metal ions including Fe^{3+}, Sb^{3+}, and Bi^{3+} are inserted into the Cs_3BiBr_6 perovskite lattice, which triggers a lattice reconstruction from the Cs_3BiBr_6 phase to the $Cs_3Bi_2Br_9$ phase. We further investigate the spin-phonon coupling and magneto-phonon response in the iron-doped bismuth halide (Fe:CBBr) perovskites. In the temperature-dependent Raman measurements, we notice a softening of the phonon frequency below ~50 K, indicating the emergence of the spin-phonon coupling. Furthermore, the Raman peak shifting to a lower frequency under an applied magnetic field at around 13 K is observed using magnetic-field-dependent Raman measurements. The observed spin-phonon coupling and magneto-phonon response in the Fe:CBBr perovskites suggest interesting spin physics and the potential of developing spin-related devices in metal halide perovskites.

RESULTS AND DISCUSSION

Synthesis and Characterizations of Cs_3BiBr_6 and Fe:CBBr Perovskites. Ultrathin Cs_3BiBr_6 perovskite derivatives are synthesized via the CVD method (see details in the Methods, and Figure S1).[16] The Cs_3BiBr_6 phase of the perovskite products is confirmed by the Raman spectra, showing a predominant peak at 158 cm^{-1} and the secondary characteristic peak at 131 cm^{-1} assigned to the Bi−Br stretching (Figure S2). These results are consistent with the Raman spectra of the Cs_3BiBr_6 perovskites in bulk and nanocrystal phases in previously reported works.[24,25] The optical image shows the triangular Cs_3BiBr_6 flakes with a lateral size ranging from around 10 to over 100 μm (Figures 1a and S3). Atomic force microscopy (AFM) images show the morphology of the Cs_3BiBr_6 flake, and the inserted height profile determines the thickness of 27 nm of the selected Cs_3BiBr_6 flake (Figure 1b). AFM and scanning electron microscopy (SEM) images (Figure S4) both show a well-defined triangular shape, presumably indicating the high crystalline quality of the Cs_3BiBr_6 perovskites prepared by the CVD approach.

Iron-doped Fe:CBBr perovskites are prepared via a postsynthetic iron(III) bromide ($FeBr_3$) vapor treatment to the CVD-grown Cs_3BiBr_6 perovskites (see details in the Methods, and Figure S5). To clearly show the lattice and composition change, we characterized the perovskite flakes treated by the metal halide vapors for 3 h. The Raman spectrum of the Fe:CBBr perovskites shows the peak shifting from 158 to 165 cm^{-1} and a new peak appearing at 190 cm^{-1}, which are the characteristic peaks of the Bi−Br stretching in the $Cs_3Bi_2Br_9$ phase (Figure 1c).[26] The Raman mapping of the peak at 190 cm^{-1} further demonstrates the horizontal distribution of the $Cs_3Bi_2Br_9$ phase in the perovskite flake

https://doi.org/10.1021/acsnano.4c03216
ACS Nano 2024, 18, 12560−12568

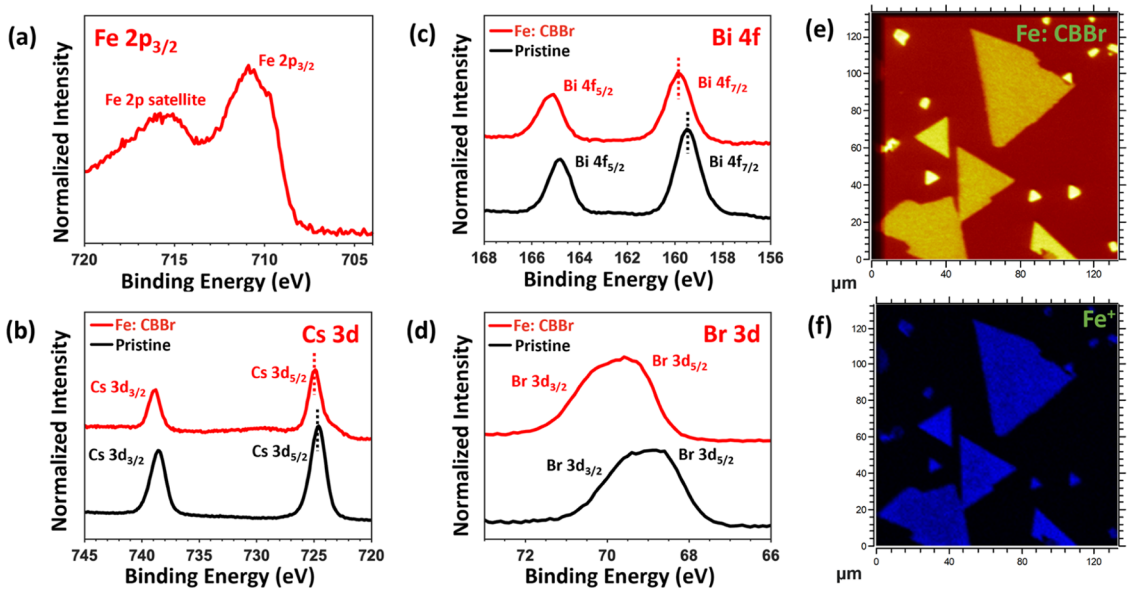

Figure 2. XPS scans of (a) Fe $2p^3$ of the Fe:CBBr perovskite and (b) Cs 3d, (c) Bi 4f, and (d) Br 3d of Fe:CBBr (red) and pristine Cs_3BiBr_6 (black) perovskites. (e) Total ion and (f) Fe^+ images of the Fe:CBBr perovskites obtained using ToF-SIMS.

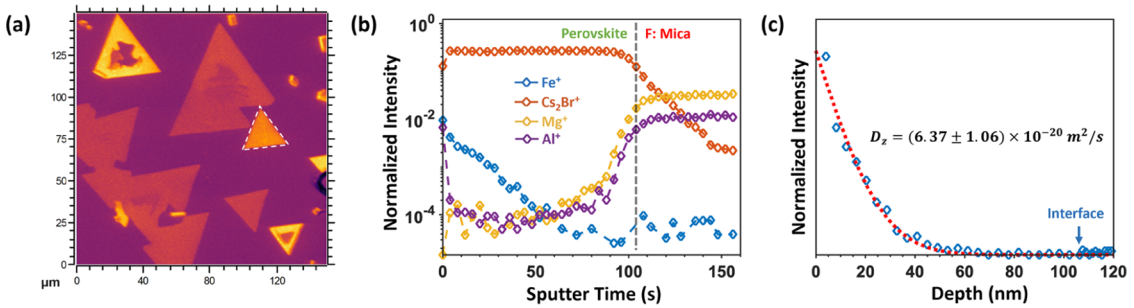

Figure 3. (a) Summarized ToF-SIMS images of the total ion from the surface to the substrate obtained on Fe:CBBr perovskites (1 h). The marked flake is selected to extract the depth profile from this specific region of interest. (b) Depth profile of the selected flake. The perovskite/F:mica interface is defined at the 50% intensity of Cs_2Br^+. The dashed line indicates the perovskite/F:mica interface. (c) Diffusivity of the iron ion in the Fe:CBBr perovskites (1 h). The *x*-axis is converted from the sputter time to the depth after determining the sputter speed. The normalized Fe^+ intensity depth profile (blue diamonds) is fitted with Fick's second law (dashed red line). The blue arrow indicates the perovskite/F:mica interface.

(Figures 1d and S6). Such a lattice structure transition is also observed in the antimony(III) bromide ($SbBr_3$) and bismuth-(III) bromide ($BiBr_3$) insertion reactions with the Cs_3BiBr_6 perovskites (Figure S7). Notably, besides the peak shifts from 158 to 165 cm^{-1} and the emerging peak at 190 cm^{-1} indicating the lattice structure transition, another new peak appears at 206 cm^{-1}, which can be assigned to the Sb−Br stretching (Figure S7a).[27] The lattice reconstruction mechanism from the Cs_3BiBr_6 phase to the $Cs_3Bi_2Br_9$ phase has been proposed and it shows that $BiBr_3$ inserted into the isolated $[BiBr_6]^{3-}$ octahedral in the Cs_3BiBr_6 nanocrystal induces the reconstruction to form the $[Bi_2Br_9]^{3-}$ layered framework and yield the $Cs_3Bi_2Br_9$ phase (Figure S8).[24] We postulate that this could be a universal mechanism for introducing various trivalent metal halides into the Cs_3BiBr_6 lattice. The lattice reconstruction process induced by the metal ion doping could be beneficial for the tunable band energy level and enable exotic optical properties.

Confirmation of the Iron Ion Doping. The detailed chemical composition of Fe:CBBr perovskites has been subsequently studied by X-ray photoelectron spectroscopy (XPS) and time-of-flight secondary ion mass spectrometry (ToF-SIMS) techniques. The Fe $2p_{3/2}$ scan confirms the successful Fe^{3+} doping with the binding energy of 710.64 eV (Figure 2a). The binding energies of Cs $3d_{5/2}$, Bi $4f_{7/2}$, and Br $3d_{5/2}$ in Fe:CBBr perovskites are located at 724.93, 159.87, and 69.42 eV, respectively (Figure 2b−d). Those binding energies show peak shifts in the Cs $3d_{5/2}$, Bi $4f_{7/2}$, and Br $3d_{5/2}$ spectra of the pristine Cs_3BiBr_6 perovskites located at 724.65, 159.48, and 68.71 eV, respectively, which indicates that the doped iron ions significantly change the chemical environment surrounding the Cs_3BiBr_6 lattices. The successful metal ion insertion of Sb^{3+} is also confirmed in the Sb:CBBr perovskites (Figure S9a). The binding energies of Sb $3d_{5/2}$ and $3d_{3/2}$ peaks are located at 530.82 and 540.16 eV, which is consistent with the previously reported Sb-based perovskites.[28] Small peaks at 528.67 and 538.01 eV are thought to be originated from the elemental Sb. The reduced elemental metal component is commonly observed in metal halide perovskites.[29,30] The peak at 532.03 eV can be assigned to oxygen from environmental contaminants. Cs 3d, Bi 4f, and Br 3d spectra of both Sb:CBBr and Bi:CBBr perovskites demonstrate negligible peak shifts from the pristine Cs_3BiBr_6 perovskites (Figure S10). We assume that the chemical similarity of the doped Fe^{3+}, Sb^{3+},

https://doi.org/10.1021/acsnano.4c03216
ACS Nano 2024, 18, 12560−12568

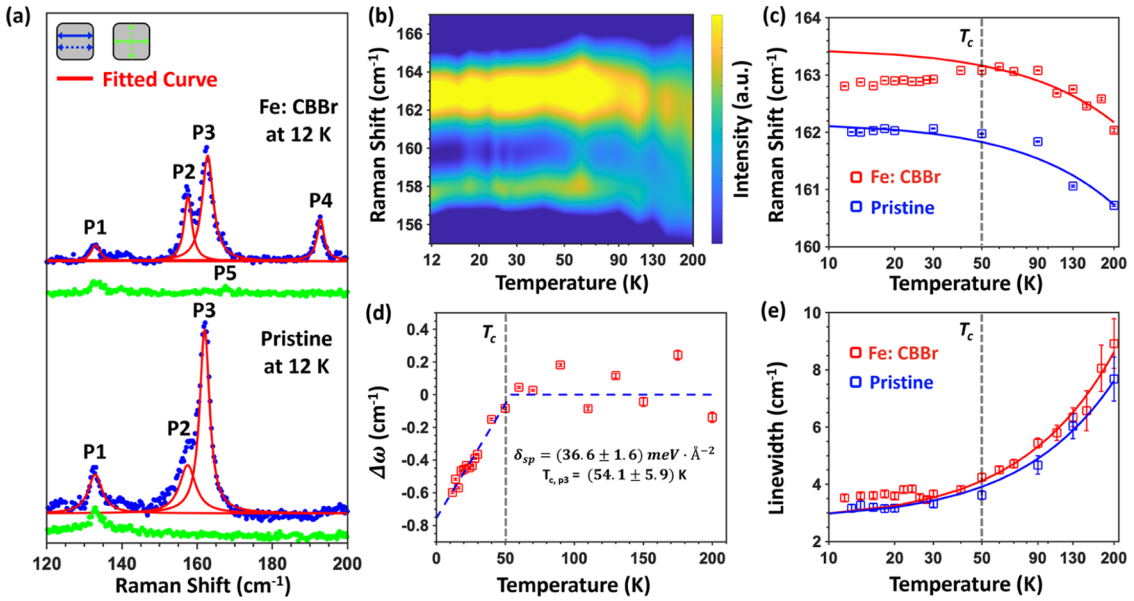

Figure 4. (a) Linearly polarized Raman spectra of the Fe:CBBr and pristine Cs_3BiBr_6 perovskites. Blue and green dots represent linearly parallel and crossed channels. Red solid lines are the Lorentzian fitting of the peaks in the linearly parallel channels. (b) Contour mapping of the temperature-dependent Raman spectra of P2 and P3. (c) Temperature-dependent Raman shifts of P3 in the Fe:CBBr (red) and pristine Cs_3BiBr_6 (blue) perovskites with an error bar. Solid lines are the fitted anharmonic model. (d) Raman shift deviation $\Delta\omega$ from the anharmonic fitting vs temperature of P3 in the Fe:CBBr perovskite. The spin-phonon coupling strength is extracted from the mean field model (dashed blue line). (e) Temperature-dependent line width of P3 of the Fe:CBBr (red) and pristine Cs_3BiBr_6 (blue) perovskites with an error bar. Solid lines are the fitted anharmonic model. The dashed gray lines indicate the approximate critical temperature of ~50 K.

and Bi^{3+} ions to the pristine Bi^{3+} ions led to the variations in peak shifts. We further performed the ToF-SIMS study to investigate the distribution of the doped metal ions (Figures 2e,f, and S11). Fe^+ signals are mainly observed from the perovskite flakes, indicating the successful doping of iron ions (Figure 2f). The ToF-SIMS images also show a uniform distribution of doped iron ions in the selected perovskite flakes.

Distribution and Diffusion of the Doped Iron Ions. The iron doping process can be controlled by reaction time and monitored by Raman spectra (Figure S12). Considering that peak intensities can depend on the thickness of the perovskite flakes, we focus on the position change of the Raman peaks at around 160 cm^{-1}. At the intermediate state (1 and 1.5 h), the peaks can be split into two peaks at 158 and 165 cm^{-1}, indicating the coexistence of the Cs_3BiBr_6 and $Cs_3Bi_2Br_9$ phases. A new peak from the Fe−Br stretching appears at 202 cm^{-1} in Fe:CBBr (6 h),[31] suggesting the accumulation of the iron ions due to the long reaction time. The vertical distribution of the doped iron ions is analyzed by ToF-SIMS (Figures 3 and S13). The depth profile (Figure 3b) of the selected Fe:CBBr (1 h) flake, as shown in Figure 3a, shows the vertical distribution of the species from the perovskite (Cs_2Br^+ and Fe^+) and the substrate (Mg^+ and Al^+). In contrast to the relatively uniform distribution of Cs_2Br^+ in the perovskite, Fe^+ from the doped iron ions demonstrates a gradient distribution attributed to the diffusion process. We further extract the information on the vertical Fe^+ distribution in the Fe:CBBr perovskite (1 h) from its depth profile to show the diffusion of the doped iron ions alongside the depth of the perovskite flake (Figure 3c). We could subsequently evaluate the average vertical diffusivity of the doped iron ions in the Fe:CBBr samples. To simplify the calculation, we only focus on the metal ion diffusion process in the Cs_3BiBr_6 phase and apply the semi-infinite diffusion model with Fick's second law to determine the iron ion diffusion coefficient in the Fe:CBBr samples. Based on the fitting result of the Fe:CBBr (1 h) sample, the diffusion coefficient at 80 °C is $6.37 \pm 1.06 \times 10^{-20}$ m^2/s. From the depth profiles of the doped iron ions in the Fe:CBBr (0.5/1.5/3 h) samples (Figure S14), we notice that Fe:CBBr (0.5 h) shows a low doping level, while Fe:CBBr (1.5 and 3 h) shows a saturated iron ion distribution and high doping levels where the diffusion may reach the perovskite−substrate interface and cannot be considered the semi-infinite diffusion model. Taking account of the variations, we could estimate the average vertical diffusion coefficient of the doped iron ions in the Fe:CBBr perovskites to be in the order of 10^{-20} m^2/s, which is lower than the halide anion diffusion coefficients (10^{-19} m^2/s) in $MAPbI_3$[32] and other two-dimensional (2D) lead halide perovskites.[33]

Spin-Phonon Coupling in Fe:CBBr. Next, we investigate the spin-phonon coupling of the Fe:CBBr (1.5 h) sample in which sufficient metal ions penetrate through the entire thickness using temperature-dependent Raman spectroscopy from 200 to around 12 K (Figures S15 and S16). Comparing the spectra of Fe:CBBr and pristine Cs_3BiBr_6 at low temperature under linearly parallel polarization (both the incident and scattered light are vertically polarized), four peaks at around 133 cm^{-1} (P1), 158 cm^{-1} (P2), 163 cm^{-1} (P3), and 193 cm^{-1} (P4) can be observed in the Fe:CBBr perovskites, while P4 is absent in pristine perovskites (Figure 4a). P4 represents the $Cs_3Bi_2Br_9$ phase similar to the room-temperature spectrum (Figure 1c). In addition, under linearly crossed polarization, we found another peak at around 167 cm^{-1} (P5) in the spectrum of the Fe:CBBr perovskite, which also comes from the $Cs_3Bi_2Br_9$ phase and merges into peak P3 in the spectrum from the linearly parallel channel. Notably, the peak at 158 cm^{-1} shown at room temperature (Figure S17) consists

https://doi.org/10.1021/acsnano.4c03216
ACS Nano 2024, 18, 12560−12568

of two peaks (P2 and P3) in both doped and pristine samples, whose separation appears to be independent from temperature (Figure 4b), indicating that both are intrinsic to the Cs_3BiBr_6 phase. As all of our targeted phonon modes are shown in the spectra from the linearly parallel channel, the following temperature-dependent Raman analysis is based on the spectra taken in the linearly parallel channel.

Qualitatively different temperature dependences between the Raman spectra of the Fe:CBBr and pristine perovskites have been observed. We initially focus on the predominant peak P3 representing the phonon behavior in the Cs_3BiBr_6 phase. The contour mapping shows the phonon frequency change of P3 as a function of the temperature (Figure 4b). As the temperature decreases from 200 to 50 K, the phonon frequency increases. Below 50 K, the phonon frequency stops increasing and reduces to a lower value, which is anomalous compared to pure Cs_3BiBr_6 (Figure 4c). The difference suggests that the phonon frequency softening in Fe:CBBr could be induced by the doped iron ions. The temperature-dependent Raman shift plot at P3 demonstrates the deviation arising below ~50 K from the anharmonic fitting:

$$\omega(T) = \omega(0) - A\left(1 + \frac{2}{e^{\hbar\omega(0)/2k_BT} - 1}\right) \quad (1)$$

where $\omega(0)$ is the phonon frequency at zero-temperature, A is the coefficient corresponding to the 3-phonon scattering strength, $\hbar$ is the reduced Planck constant, and k_B is the Boltzmann's constant. A deviation that continuously increases (Figure 4d) as temperature decreases usually implies a second-order phase transition, such as the appearance of a magnetic order, which has been reported in various magnets including $MnBi_2Te_4$ and Fe_3GeTe_2.[10,11] Previously, introducing iron into the MHP structures has been proven to bring spin and magnetic order in iron-magnetized MHP[17] and antiferromagnetic pure iron halide-based perovskites.[34,35] However, a phonon frequency shift may also be a signature of increasing spin fluctuations manifesting through spin-phonon coupling, like P3, P1, and P2 also show the reduced phonon frequencies deviating from the anharmonic fitting below ~40−50 K (Figure S18a,c). Hence, it is clear that the doped iron ions introduce spin to the nonmagnetic perovskites and induce spin-phonon coupling in the Fe:CBBr perovskites. Electron paramagnetic resonance (EPR) measurements (Figure S20) further confirm the presence of Fe^{3+} and demonstrate that the Fe^{3+} doping effect induces the spin interactions in bismuth halide perovskites (see more discussion in the Supporting note).

Spin-phonon coupling can be quantified by the phonon frequencies deviating from the anharmonic model. We extract the spin-phonon coupling strength δ_{sp} and critical temperature T_c of the spin-phonon coupling state following the reported modified mean field model (Figure 4d)[10,36]

$$\Delta\omega = \frac{-\delta_{sp}}{2\mu\omega}\left(1 - \frac{T}{T_c}\right), \text{ when } (T < T_c) \quad (2)$$

where μ is the mode reduced mass. The spin-phonon coupling strength δ_{sp} of P3 is calculated to be (36.6 ± 1.6) meV/Å^2 and the critical temperature T_c is determined to be (54.1 ± 5.9) K. Following the same rules, we extract the spin-phonon coupling strengths δ_{sp} of P1 and P2 of (23.8 ± 5.3) and (24.9 ± 3.9) meV/Å^2, respectively (Figure S18b,d). The critical temperatures T_c obtained from P1 and P2 are (37.2 ± 16.0) and (47.3 ± 14.9) K, respectively. Due to the relatively small errors from the phonon mode P3, we consider that the critical temperature T_c = 54.1 K determined in P3 is closer to the real value. We suggest that the critical temperature T_c of tested Fe:CBBr should be approximately at ~50 K, which is also within the standard error of the T_c calculated from phonon modes P1 and P2. It is worth mentioning that since the doped iron ions are distributed with a gradient in the perovskites, the spin-phonon coupling strengths and critical temperatures we calculated are considered average values and may be meaningful only for samples with a similar iron ion distribution and concentration. It is our belief that such properties can be tuned by controlling the concentration and homogeneity of doped iron ions.

In addition to the phonon frequency, the line width of the Raman peaks (from the Lorentzian fitting) also describes the vibration properties of the phonon mode. We take the line width of P3 as an example, which will give fewer fitting errors to the anharmonic model, to further interpret the spin-phonon coupling in the Cs_3BiBr_6 phase. The Raman peak line widths of the Fe:CBBr and pristine perovskites versus temperature are plotted in Figure 4e. After fitting to the anharmonic model,

$$\Gamma(T) = \Gamma_0 + B\left(1 + \frac{2}{e^{\hbar\omega_0/2K_BT} - 1}\right) \quad (3)$$

where Γ_0 is the zero-temperature line width and B is the adjustable parameter, we observe that the line width is larger than the fitting curve below the critical temperature. In contrast to the negligible deviation from the anharmonic fitting in the pristine perovskite, the broadening of Raman peaks deviating from the anharmonic fitting in P3 also indicates the spin-phonon coupling in the Fe:CBBr perovskite induced by the doped iron ions. Meanwhile, the good anharmonic fitting of phonon frequencies and line widths in the pristine perovskites suggests that any possible structural phase transition does not contribute to the Raman anomaly in the testing temperature range and will not interfere with our analysis of the spin-phonon coupling.

The phonon P4 represents the $Cs_3Bi_2Br_9$ phase in the Fe:CBBr perovskite. Comparing with the phonon modes in the Cs_3BiBr_6 phase, we observe spin-phonon coupling arising at around 50 K as well, indicated by the reduced phonon frequencies (Figure S19a). We extract the spin-phonon coupling constant of P4 to be (18.5 ± 4.2) meV/Å^2, comparable to that of the phonon modes in the Cs_3BiBr_6 phase (Figure S19b). The critical temperature T_c is further determined to be (47.3 ± 20.9) K. The increased line width below the critical temperature deviating from the anharmonic fitting can also be observed, indicating the occurrence of the spin-phonon coupling (Figure S19c). We therefore believe that the Fe atoms also doped into the $Cs_3Bi_2Br_9$ phase and led to the observed spin-phonon coupling.

Magneto-Phonon Response in Fe:CBBr. Finally, to investigate the magneto-phonon response in the Fe:CBBr perovskites, we apply a magnetic-field-dependent Raman spectroscopy technique. In the circular polarization mode, phonon modes P2, P3, and P4 are active in LL and RR channels (cocircularly polarized) but become weak or silent in LR and RL channels (Figure S21). In contrast, P1 and P5 appear in LR and RL channels but are weak or overwhelmed by other peaks in the LL and RR channels. The Raman spectra of P2, P3, and P4 in LL and RR channels (Figure S22), as well as P1 and P5 shown in LR and RL channels under the

https://doi.org/10.1021/acsnano.4c03216
ACS Nano 2024, 18, 12560−12568

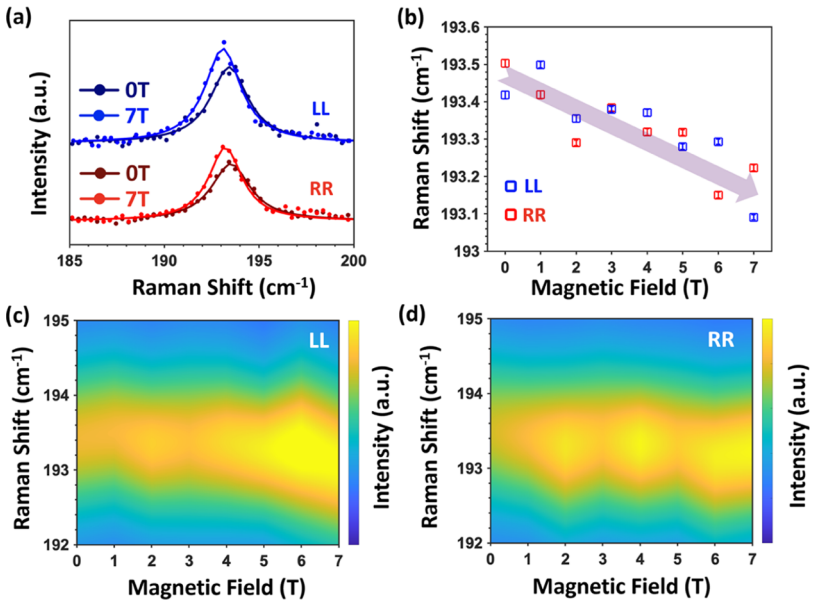

Figure 5. Magnetic-field-dependent Raman of P4 in the Fe:CBBr perovskite. (a) Comparison of the Raman spectra at 0T and 7T in the LL and RR channels. Solid lines are the Lorentzian fittings. (b) Raman shifts versus applied magnetic field in the LL (red) and RR (blue) channels. The transparent purple arrow is guided to the eyes to show the overall phonon frequency softening under an applied magnetic field. Contour mapping of the magnetic-field-dependent Raman in (c) LL and (d) RR channels.

sweeping magnetic field from 0T to 7T, are available in Figures S22 and S23, respectively. By direct comparison of the spectra at 0T and 7T, P4 shows a clear shift to the lower phonon frequency at 7T in both LL and RR channels (Figure 5a). We further observed an overall phonon frequency softening under a sweeping magnetic field, as summarized in Figure 5b. The contour mappings exhibit the magneto-phonon response to the applied magnetic field, especially the magnetic-field-dependent phonon frequency softening, in both LL (Figure 5c) and RR (Figure 5d) channels. By contrast, P2 (Figure S24a) and P3 (Figure S24b) do not show a clear magnetic-field-dependent phonon frequency response in the LL and RR channels. In the LR and RL channels, we find that P1 (Figure S24c) and P5 (Figure S24d) also demonstrate the phonon frequency softening under the applied magnetic field. Overall, the magnetic-field-induced frequency shifts are indications of the magnitude of spin-phonon coupling strengths of each mode. We postulate that when the applied field modifies the orientation and interaction of spins, the interatomic spring constants and the frequency of each mode changes accordingly, in a similar mechanism as the static magneto-striction effect.[37,38] Although nonmagnetic materials may also exhibit finite magnetostriction,[39,40] the observed large magnitude of phonon softening on the order of 0.1% above 4T is more consistent with the materials' strong spin exchange interaction and magnetic order.[41,42] We have not observed any saturation or hysteresis in either the helicity or the intensity of the field-dependent Raman spectra, implying that the spin order, if any, is unlikely to be ferromagnetism. This agrees with the antiferromagnetic exchange between iron spins observed in pure $Cs_3Fe_2Br_9$, but the onset of spin correlation occurs at a much higher temperature in doped ultrathin films than pure crystals.[34] Therefore, our result implies that exchange interaction increases as a function of the Fe—Fe distance, and the magnetic order can potentially be stabilized at a higher temperature with an optimal doping level.

CONCLUSIONS

In summary, we demonstrate that the methodology of synthesizing ultrathin Fe:CBBr perovskites through the $FeBr_3$ vapor treatment was transferred to CVD-grown Cs_3BiBr_6. This facile doping protocol employing the metal halide insertion reaction can be versatile to the various metal ions more than the introduced Fe^{3+}, Sb^{3+}, and Bi^{3+}, and it can be further developed for other vapor- or solution-phase-based synthesis approaches. The successful metal ion doping and simultaneous lattice structure reconstruction from the Cs_3BiBr_6 phase to the $Cs_3Bi_2Br_9$ phase are confirmed by XPS, ToF-SIMS, and Raman techniques. Doping and diffusion processes of the iron ions analyzed by Raman spectra and ToF-SIMS depth profiles suggest that the doping process can be controlled and could benefit practical applications. The compositional engineering of the bismuth halide perovskites will provide tremendous opportunities for tuning optical properties in such perovskites in future work. We further confirm the occurrence of spin-phonon coupling in Fe:CBBr by applying temperature-dependent and polarization-resolved magnetic-field-dependent Raman spectroscopies. By interpreting the temperature-dependent phonon behaviors, we observe that the spin-phonon coupling arises at ~50 K in both the Cs_3BiBr_6 phase and the $Cs_3Bi_2Br_9$ phase. Magnetic field softening of phonons further confirms that the doped iron ions induce spin momentum and spin exchange interactions in the Fe:CBBr perovskites. The spin-phonon coupling and magneto-phonon response provide the pathway toward spin- and magnetic-related devices in metal halide perovskites.

METHODS

Materials. Iron(III) bromide ($FeBr_3$, 98%) was purchased from Sigma-Aldrich. Cesium bromide (CsBr, 99%), bismuth(III) bromide ($BiBr_3$, 99%), and antimony(III) bromide ($SbBr_3$, 99.5%) were purchased from Thermal Scientific. All chemicals were used as received.

https://doi.org/10.1021/acsnano.4c03216
ACS Nano 2024, 18, 12560−12568

CVD Growth of the Cs_3BiBr_6 Perovskites. 300 mg portion of CsBr and 200 mg of $BiBr_3$ were mixed and placed at the upstream side of the quartz boat. F:mica substrates were placed about 3 cm behind the precursor powders. The CVD furnace tube was purged by 100 sccm N_2/H_2 gas for 1 h, followed by sequentially heating up to 630 °C in 20 min, maintaining the temperature at 630 °C for 1 h and naturally cooling down to the room temperature.

Metal Ion Insertion Reactions. As-synthesized Cs_3BiBr_6 perovskites on F:mica substrates and around 20 mg of metal bromide powders ($FeBr_3$, $SbBr_3$, and $BiBr_3$) were charged in the 20 mL vials. Then, the capped vials were heated at 80 °C for $FeBr_3$ and $SbBr_3$ and at 120 °C for $BiBr_3$ for the desired reaction times. To avoid quenching of the precursor vapor, the vials were cooled down to 50 °C (80 °C for $BiBr_3$) before removing from the hot plate. The reactions were performed in the argon-filled glovebox.

Characterization of the Bismuth Halide Perovskites. Atomic force microscopy (AFM) was performed with a Park AFM NX20 microscope. Room-temperature Raman spectra and mappings were collected by a Renishaw inVia confocal Raman microscope with 532 nm laser excitation. Scanning electron microscopy (SEM) images were collected from the FEI Helios NanoLab 660 DualBeam system that integrates advanced scanning electron microscopy. X-ray photoelectron spectroscopy (XPS) was performed on a PHI Quantera XPS instrument using a focused monochromatic Al Kα X-ray (1486.7 eV) source for excitation. The 50 W, 15 kV, and 200 μm diameter X-rays were shot on the sample. Low-energy electrons and Ar^+ ions were conducted for specimen neutralization in each measurement. The XPS survey scan spectra in the 1100−0 eV binding energy range were recorded in 0.5 eV steps with a pass energy of 140 eV. High-resolution scan spectra were recorded in 0.1 eV steps with a pass energy of 26 eV.

ToF-SIMS Analysis. ToF-SIMS analysis was performed using a ToF-SIMS NCS instrument, which combines a ToF-SIMS instrument (ION-ToF GmbH, Münster, Germany) and an in situ scanning probe microscope (NanoScan, Switzerland). Three-dimensional (3D) analysis of perovskites by ToF-SIMS was conducted by using Bi_3^+ (30 keV) as the primary probe in positive polarization mode for analysis and Cs^+ (2 keV) for sputtering. The analysis area with a measured current of 0.2 pA was placed in the center of the sputter crater (300 × 300 μm^2) with a typical current around 125 nA. The beams were operated in noninterlaced mode, alternating 2 analysis cycles and 20 sputtering cycles (corresponding to 31.67 s) followed by a pause of 5 s for the charge compensation with an electron flood gun. An adjustment of the charge effects was operated using a surface potential. During depth profiling, the cycle time was fixed to 100 μs (corresponding to m/z = 0−839 a.m.u mass range).

Raman Measurements. Raman spectra were taken using a Horiba LabRAM HR Evolution Raman microscope equipped with an 1800 grooves/mm grating and a thermoelectrically cooled CCD. A 633 nm laser with backscattering geometry was used and focused to a spot size of ~3 μm using a long working distance 40× objective lens. Laser power was kept below ~0.5 mW to avoid a heating effect. A closed-cycle helium cryostat (from Cryo Industries, Inc.) with an optical window was used for variable-temperature Raman measurements. All thermal cycles were performed in a vacuum condition with the base pressure below 7 × 10^7 Torr. A cryogen-free 7T superconducting magnet system (also from Cryo Industries, Inc.) was interfaced with a low-temperature cryostat for magneto-Raman measurements.

Electron Paramagnetic Resonance (EPR) Measurements. EPR was performed on an X-band Bruker Elexsys E500 spectrometer operating in a continuous wave regime at 9.38 GHz. The modulation frequency used was 100 kHz with a 4 G amplitude. The sample in the form of thin sheets was stacked at the bottom of an SP Wilmad-LabGlass clear fused quartz tube with a 4 mm outer diameter and a 250 mm length. The low-temperature 40 and 5 K spectra were collected upon cooling the sample by connecting the liquid helium flow cryostat.

ASSOCIATED CONTENT

Supporting Information

The Supporting Information is available free of charge at https://pubs.acs.org/doi/10.1021/acsnano.4c03216.

Additional optical images, Raman spectra, SEM images, XPS scans, and ToF-SIMS analysis of the ultrathin bismuth halide perovskites; schematics of the CVD growth of Cs_3BiBr_6, the metal halide insertion reaction setup, and lattice reconstruction; temperature-dependent Raman measurements of Cs_3BiBr_6 and Fe:CBBr perovskites; magnetic-field-dependent Raman measurements of Fe:CBBr perovskites; EPR measurements of Fe:CBBr perovskites; and a supporting note of the determination of spin-phonon coupling and critical temperature (PDF)

AUTHOR INFORMATION

Corresponding Authors

Hanyu Zhu − *Department of Materials Science and NanoEngineering, Rice University, Houston, Texas 77005, United States;* orcid.org/0000-0003-3376-5352; Email: hanyu.zhu@rice.edu

Rui He − *Department of Electrical and Computer Engineering, Texas Tech University, Lubbock, Texas 79409, United States;* orcid.org/0000-0002-2368-7269; Email: Rui.He@ttu.edu

Jun Lou − *Department of Materials Science and NanoEngineering, Rice University, Houston, Texas 77005, United States;* orcid.org/0000-0002-4351-9561; Email: jlou@rice.edu

Authors

Yifeng Liu − *Department of Materials Science and NanoEngineering, Rice University, Houston, Texas 77005, United States*

Qing Ai − *Department of Materials Science and NanoEngineering, Rice University, Houston, Texas 77005, United States;* orcid.org/0000-0002-6086-5431

Gaihua Ye − *Department of Electrical and Computer Engineering, Texas Tech University, Lubbock, Texas 79409, United States*

Zhipeng Ye − *Department of Electrical and Computer Engineering, Texas Tech University, Lubbock, Texas 79409, United States*

Jakub Hrubý − *National High Magnetic Field Laboratory, Tallahassee, Florida 32310, United States*

Fan Wang − *Department of Materials Science and NanoEngineering, Rice University, Houston, Texas 77005, United States*

Tomas Orlando − *National High Magnetic Field Laboratory, Tallahassee, Florida 32310, United States*

Yuguo Wang − *Department of Materials Science and NanoEngineering, Rice University, Houston, Texas 77005, United States*

Jiaming Luo − *Applied Physics Program, Smalley-Curl Institute, Rice University, Houston, Texas 77005, United States;* orcid.org/0009-0007-8362-9558

Qiyi Fang − *Department of Materials Science and NanoEngineering, Rice University, Houston, Texas 77005, United States*

Boyu Zhang − *Department of Materials Science and NanoEngineering, Rice University, Houston, Texas 77005, United States*
Tianshu Zhai − *Department of Materials Science and NanoEngineering, Rice University, Houston, Texas 77005, United States*
Chen-yang Lin − *Department of Materials Science and NanoEngineering, Rice University, Houston, Texas 77005, United States*
Clyde Xu − *Department of Materials Science and NanoEngineering, Rice University, Houston, Texas 77005, United States*
Yifan Zhu − *Department of Materials Science and NanoEngineering, Rice University, Houston, Texas 77005, United States;* orcid.org/0000-0002-9816-5764
Tanguy Terlier − *SIMS Laboratory, Shared Equipment Authority, Rice University, Houston, Texas 77005, United States;* orcid.org/0000-0002-4092-0771
Stephen Hill − *National High Magnetic Field Laboratory, Tallahassee, Florida 32310, United States; Department of Physics, Florida State University, Tallahassee, Florida 32306, United States;* orcid.org/0000-0001-6742-3620

Complete contact information is available at: https://pubs.acs.org/10.1021/acsnano.4c03216

Author Contributions

[▽]Y.L. and Q.A. contributed equally to this work.

Notes

The authors declare no competing financial interest.

ACKNOWLEDGMENTS

This work is mainly supported by the Welch Foundation Grant C-1716. G.Y., Z.Y., and R.H. acknowledge the support from the NSF Grant No. DMR-2104036. J.L. and H.Z. acknowledge the Welch Foundation Grant C-2128. Work performed at the National High Magnetic Field Laboratory is supported by the US National Science Foundation (DMR-2128556) and the State of Florida. Characterizations including AFM, SEM, ambient Raman, ToF-SIMS, and XPS were conducted using resources of the Shared Equipment Authority at Rice University. ToF-SIMS analysis was carried out with support provided by the National Science Foundation CBET-1626418. Y.L. dedicates this work to the memory of Professor Marc Robert (1950−2022).

REFERENCES

(1) Wehrenfennig, C.; Eperon, G. E.; Johnston, M. B.; Snaith, H. J.; Herz, L. M. High Charge Carrier Mobilities and Lifetimes in Organolead Trihalide Perovskites. *Adv. Mater.* **2014**, *26*, 1584−1589.
(2) Alcocer, M. J. P.; Leijtens, T.; Herz, L. M.; Petrozza, A.; Snaith, H. J. Electron-Hole Diffusion Lengths Exceeding Trihalide Perovskite Absorber. *Science* **2013**, *342*, 341−344.
(3) Ravi, V. K.; Markad, G. B.; Nag, A. Band Edge Energies and Excitonic Transition Probabilities of Colloidal CsPbX3 (X = Cl, Br, I) Perovskite Nanocrystals. *ACS Energy Lett.* **2016**, *1*, 665−671.
(4) Kepenekian, M.; Robles, R.; Katan, C.; Sapori, D.; Pedesseau, L.; Even, J. Rashba and Dresselhaus Effects in Hybrid Organic-Inorganic Perovskites: From Basics to Devices. *ACS Nano* **2015**, *9*, 11557−11567.
(5) Long, G.; Jiang, C.; Sabatini, R.; Yang, Z.; Wei, M.; Quan, L. N.; Liang, Q.; Rasmita, A.; Askerka, M.; Walters, G.; Gong, X.; Xing, J.; Wen, X.; Quintero-Bermudez, R.; Yuan, H.; Xing, G.; Wang, X. R.; Song, D.; Voznyy, O.; Zhang, M.; Hoogland, S.; Gao, W.; Xiong, Q.; Sargent, E. H. Spin Control in Reduced-Dimensional Chiral Perovskites. *Nat. Photonics* **2018**, *12*, 528−533.
(6) Hsiao, Y. C.; Wu, T.; Li, M.; Hu, B. Magneto-Optical Studies on Spin-Dependent Charge Recombination and Dissociation in Perovskite Solar Cells. *Adv. Mater.* **2015**, *27*, 2899−2906.
(7) Lee, J. H.; Fang, L.; Vlahos, E.; Ke, X.; Jung, Y. W.; Kourkoutis, L. F.; Kim, J. W.; Ryan, P. J.; Heeg, T.; Roeckerath, M.; Goian, V.; Bernhagen, M.; Uecker, R.; Hammel, P. C.; Rabe, K. M.; Kamba, S.; Schubert, J.; Freeland, J. W.; Muller, D. A.; Fennie, C. J.; Schiffer, P.; Gopalan, V.; Johnston-Halperin, E.; Schlom, D. G. A Strong Ferroelectric Ferromagnet Created by Means of Spin-Lattice Coupling. *Nature* **2010**, *466*, 954−958.
(8) Mochizuki, M.; Furukawa, N.; Nagaosa, N. Theory of Spin-Phonon Coupling in Multiferroic Manganese Perovskites RMnO3. *Phys. Rev. B* **2011**, *84*, No. 144409, DOI: 10.1103/PhysRevB.84.144409.
(9) Son, J.; Park, B. C.; Kim, C. H.; Cho, H.; Kim, S. Y.; Sandilands, L. J.; Sohn, C.; Park, J. G.; Moon, S. J.; Noh, T. W. Unconventional Spin-Phonon Coupling via the Dzyaloshinskii−Moriya Interaction. *npj Quantum Mater.* **2019**, *4*, No. 17, DOI: 10.1038/s41535-019-0157-0.
(10) Choe, J.; Lujan, D.; Rodriguez-Vega, M.; Ye, Z.; Leonardo, A.; Quan, J.; Nunley, T. N.; Chang, L. J.; Lee, S. F.; Yan, J.; Fiete, G. A.; He, R.; Li, X. Electron-Phonon and Spin-Lattice Coupling in Atomically Thin Layers of MnBi2Te4. *Nano Lett.* **2021**, *21*, 6139−6145.
(11) Du, L.; Tang, J.; Zhao, Y.; Li, X.; Yang, R.; Hu, X.; Bai, X.; Wang, X.; Watanabe, K.; Taniguchi, T.; Shi, D.; Yu, G.; Bai, X.; Hasan, T.; Zhang, G.; Sun, Z. Lattice Dynamics, Phonon Chirality, and Spin−Phonon Coupling in 2D Itinerant Ferromagnet Fe3GeTe2. *Adv. Funct. Mater.* **2019**, *29*, No. 1904734, DOI: 10.1002/adfm.201904734.
(12) Wang, M.; Xu, H.; Wu, T.; Ambaye, H.; Qin, J.; Keum, J.; Ivanov, I. N.; Lauter, V.; Hu, B. Optically Induced Static Magnetization in Metal Halide Perovskite for Spin-Related Optoelectronics. *Adv. Sci.* **2021**, *8*, No. 2004488, DOI: 10.1002/advs.202004488.
(13) Zhao, W.; Su, R.; Huang, Y.; Wu, J.; Fong, C. F.; Feng, J.; Xiong, Q. Transient Circular Dichroism and Exciton Spin Dynamics in All-Inorganic Halide Perovskites. *Nat. Commun.* **2020**, *11*, No. 5665, DOI: 10.1038/s41467-020-19471-9.
(14) Li, Z.; Han, Y.; Qiao, Z. Large-Gap Quantum Anomalous Hall Effect in Monolayer Halide Perovskite. *Phys. Rev. B* **2021**, *104*, No. 205401, DOI: 10.1103/PhysRevB.104.205401.
(15) Liu, Z.; You, L.; Faraji, N.; Lin, C. H.; Xu, X.; He, J. H.; Seidel, J.; Wang, J.; Alshareef, H. N.; Wu, T. Single-Crystal Hybrid Perovskite Platelets on Graphene: A Mixed-Dimensional Van Der Waals Heterostructure with Strong Interface Coupling. *Adv. Funct. Mater.* **2020**, *30*, No. 1909672, DOI: 10.1002/adfm.201909672.
(16) Liang, J.; Fang, Q.; Wang, H.; Xu, R.; Jia, S.; Guan, Y.; Ai, Q.; Gao, G.; Guo, H.; Shen, K.; Wen, X.; Terlier, T.; Wiederrecht, G. P.; Qian, X.; Zhu, H.; Lou, J. Perovskite-Derivative Valleytronics. *Adv. Mater.* **2020**, *32*, No. 2004111, DOI: 10.1002/adma.202004111.
(17) Ning, W.; Bao, J.; Puttisong, Y.; Moro, F.; Kobera, L.; Shimono, S.; Wang, L.; Ji, F.; Cuartero, M.; Kawaguchi, S.; Abbrent, S.; Ishibashi, H.; de Marco, R.; Bouianova, I. A.; Crespo, G. A.; Kubota, Y.; Brus, J.; Chung, D. Y.; Sun, L.; Chen, W. M.; Kanatzidis, M. G.; Gao, F. Magnetizing Lead-Free Halide Double Perovskites. *Sci. Adv.* **2020**, *6*, No. eabb5381, DOI: 10.1126/sciadv.abb5381.
(18) Náfrádi, B.; Szirmai, P.; Spina, M.; Lee, H.; Yazyev, O. V.; Arakcheeva, A.; Chernyshov, D.; Gibert, M.; Forró, L.; Horváth, E. Optically Switched Magnetism in Photovoltaic Perovskite CH 3 NH 3 (Mn:Pb)I 3. *Nat. Commun.* **2016**, *7*, No. 13406, DOI: 10.1038/ncomms13406.
(19) Liang, J.; Han, X.; Yang, J. H.; Zhang, B.; Fang, Q.; Zhang, J.; Ai, Q.; Ogle, M. M.; Terlier, T.; Martí, A. A.; Lou, J. Defect-Engineering-Enabled High-Efficiency All-Inorganic Perovskite Solar Cells. *Adv. Mater.* **2019**, *31*, No. 1903448, DOI: 10.1002/adma.201903448.

(20) Pan, G.; Bai, X.; Yang, D.; Chen, X.; Jing, P.; Qu, S.; Zhang, L.; Zhou, D.; Zhu, J.; Xu, W.; Dong, B.; Song, H. Doping Lanthanide into Perovskite Nanocrystals: Highly Improved and Expanded Optical Properties. *Nano Lett.* **2017**, *17*, 8005−8011.
(21) Van der Stam, W.; Geuchies, J. J.; Altantzis, T.; Van Den Bos, K. H. W.; Meeldijk, J. D.; Van Aert, S.; Bals, S.; Vanmaekelbergh, D.; De Mello Donega, C. Highly Emissive Divalent-Ion-Doped Colloidal CsPb1-XMxBr3 Perovskite Nanocrystals through Cation Exchange. *J. Am. Chem. Soc.* **2017**, *139*, 4087−4097.
(22) Hills-Kimball, K.; Pérez, M. J.; Nagaoka, Y.; Cai, T.; Yang, H.; Davis, A. H.; Zheng, W.; Chen, O. Ligand Engineering for Mn2+ Doping Control in CsPbCl3 Perovskite Nanocrystals via a Quasi-Solid-Solid Cation Exchange Reaction. *Chem. Mater.* **2020**, *32*, 2489−2500.
(23) Shamsi, J.; Urban, A. S.; Imran, M.; De Trizio, L.; Manna, L. Metal Halide Perovskite Nanocrystals: Synthesis, Post-Synthesis Modifications, and Their Optical Properties. *Chem. Rev.* **2019**, *119*, 3296−3348.
(24) Yang, H.; Cai, T.; Liu, E.; Hills-Kimball, K.; Gao, J.; Chen, O. Synthesis and Transformation of Zero-Dimensional Cs3BiX6 (X = Cl, Br) Perovskite-Analogue Nanocrystals. *Nano Res.* **2020**, *13*, 282−291.
(25) Tran, M. N.; Cleveland, I. J.; Aydil, E. S. Resolving the Discrepancies in the Reported Optical Absorption of Low-Dimensional Non-Toxic Perovskites, Cs3Bi2Br9and Cs3BiBr6. *J. Mater. Chem. C* **2020**, *8*, 10456−10463.
(26) Valakh, M. Y.; Lisitsa, M. P.; Trilis, A. V.; Yaremko, A. M.; Peresh, E. Y. Raman Scattering in A3B2C9 Ferroelectric Crystals. *Phys. Solid State* **1997**, *39*, 1289−1291.
(27) Shi, M.; Zhou, H.; Tian, W.; Yang, B.; Yang, S.; Han, K.; Li, R.; Li, C. Lead-Free B-Site Bimetallic Perovskite Photocatalyst for Efficient Benzylic C−H Bond Activation. *Cell Rep. Phys. Sci.* **2021**, *2*, No. 100656.
(28) Zhang, J.; Yang, Y.; Deng, H.; Farooq, U.; Yang, X.; Khan, J.; Tang, J.; Song, H. High Quantum Yield Blue Emission from Lead-Free Inorganic Antimony Halide Perovskite Colloidal Quantum Dots. *ACS Nano* **2017**, *11*, 9294−9302.
(29) Liu, Y.; Zhu, Y.; Alahakoon, S. B.; Egap, E. Synthesis of Imine-Based Covalent Organic Frameworks Catalyzed by Metal Halides and in Situ Growth of Perovskite@COF Composites. *ACS Mater. Lett.* **2020**, *2*, 1561−1566.
(30) Gonzalez-Carrero, S.; Galian, R. E.; Pérez-Prieto, J. Maximizing the Emissive Properties of CH3NH3PbBr3 Perovskite Nanoparticles. *J. Mater. Chem. A* **2015**, *3*, 9187−9193.
(31) Yue, B.; Jin, X.; Zhao, P.; Zhu, M.; Zhu, L. Directed Self-Assembly of Templatable Block Copolymers by Easily Accessible Magnetic Control. *Small* **2019**, *15*, No. 1804572, DOI: 10.1002/smll.201804572.
(32) Elmelund, T.; Scheidt, R. A.; Seger, B.; Kamat, P. V. Bidirectional Halide Ion Exchange in Paired Lead Halide Perovskite Films with Thermal Activation. *ACS Energy Lett.* **2019**, *4*, 1961−1969.
(33) Akriti; Shi, E.; Shiring, S. B.; Yang, J.; Atencio-Martinez, C. L.; Yuan, B.; Hu, X.; Gao, Y.; Finkenauer, B. P.; Pistone, A. J.; Yu, Y.; Liao, P.; Savoie, B. M.; Dou, L. Layer-by-Layer Anionic Diffusion in Two-Dimensional Halide Perovskite Vertical Heterostructures. *Nat. Nanotechnol.* **2021**, *16*, 584−591.
(34) Wei, F.; Brivio, F.; Wu, Y.; Sun, S.; Bristowe, P. D.; Cheetham, A. K. Synthesis, Crystal Structure, Magnetic and Electronic Properties of the Caesium-Based Transition Metal Halide Cs3Fe2Br9. *J. Mater. Chem. C* **2018**, *6*, 3573−3577.
(35) Ishii, Y.; Narumi, Y.; Matsushita, Y.; Oda, M.; Kida, T.; Hagiwara, M.; Yoshida, H. K. Field-Induced Successive Phase Transitions in the J1-J2 Buckled Honeycomb Antiferromagnet Cs3Fe2Cl9. *Phys. Rev. B* **2021**, *103*, No. 104433, DOI: 10.1103/PhysRevB.103.104433.
(36) Olsson, K. S.; Choe, J.; Rodriguez-Vega, M.; Khalsa, G.; Benedek, N. A.; He, J.; Fang, B.; Zhou, J.; Fiete, G. A.; Li, X. Spin-Phonon Interaction in Yttrium Iron Garnet. *Phys. Rev. B* **2021**, *104*, No. L020401, DOI: 10.1103/PhysRevB.104.L020401.
(37) Poojitha, B.; Rathore, A.; Kumar, A.; Saha, S. Signatures of Magnetostriction and Spin-Phonon Coupling in Magnetoelectric Hexagonal 15R-BaMn O3. *Phys. Rev. B* **2020**, *102*, No. 134436, DOI: 10.1103/PhysRevB.102.134436.
(38) Pai, Y. Y.; Marvinney, C. E.; Feldman, M. A.; Lerner, B.; Phang, Y. S.; Xiao, K.; Yan, J.; Liang, L.; Lapano, J.; Brahlek, M.; Lawrie, B. J. Magnetostriction of α-RuCl3Flakes in the Zigzag Phase. *J. Phys. Chem. C* **2021**, *125*, 25687−25694.
(39) Kapitza, P. Magnetostriction of Diamagnetic Substances in Strong Magnetic Fields. *Nature* **1929**, *124*, 53.
(40) Laforge, A. D.; Frenzel, A.; Pursley, B. C.; Lin, T.; Liu, X.; Shi, J.; Basov, D. N. Optical Characterization of Bi2Se3 in a Magnetic Field: Infrared Evidence for Magnetoelectric Coupling in a Topological Insulator Material. *Phys. Rev. B* **2010**, *81*, No. 125120, DOI: 10.1103/PhysRevB.81.125120.
(41) Jiang, S.; Xie, H.; Shan, J.; Mak, K. F. Exchange Magnetostriction in Two-Dimensional Antiferromagnets. *Nat. Mater.* **2020**, *19*, 1295−1299.
(42) Hemberger, J.; Von Nidda, H. A. K.; Tsurkan, V.; Loidl, A. Large Magnetostriction and Negative Thermal Expansion in the Frustrated Antiferromagnet ZnCr2Se4. *Phys. Rev. Lett.* **2007**, *98*, No. 147203, DOI: 10.1103/PhysRevLett.98.147203.

https://doi.org/10.1021/acsnano.4c03216
ACS Nano 2024, 18, 12560−12568